scientific reports

Check for updates

OPEN

Novel Ni/Fe-MIL-53@ZnO nanocomposite for efficient photodegradation of aflatoxins G1 and G2

Zinat Gordi✉ & Shiva Teilaghi

The photodegradation of aflatoxins G1 and G2 (AFG1 and AFG2) is crucial for mitigating the health risks associated with these potent mycotoxins, as it enhances food safety and protects human health by reducing their persistence and bioavailability in contaminated environments. This study investigates the efficient photodegradation of AFG1 and AFG2 using a novel Bimetallic MIL-53 (Al, Ni)/ZnO nanoparticle composite as a photocatalyst. The catalyst was synthesized in two stages: Chemical synthesis of zinc oxide nanoparticles (ZnO NPs) and hydrothermal synthesis to form the composite. Optimization of a ZnO-based photocatalyst, synthesized by varying proportions of $NiCl_2{\cdot}6H_2O$ and $Al(NO_3)_3{\cdot}9H_2O$, revealed that a 0.547 g:0.864 g ratio maximized photocatalytic degradation of AFG1 and AFG2. Through experimental design, the degradation process was optimized, identifying pH 4.1, 109 mg of photocatalyst, 35 mg L^{-1} of AF concentration, and 3 mM of H_2O_2 concentration as optimal conditions. The predicted removal efficiencies for AFG1 and AFG2 were 97.43% and 98.69%, respectively. Kinetic studies utilizing the pseudo-first-order rate equation revealed rate constants of 0.058 ± 0.002 and 0.060 ± 0.003 min^{-1} for AFG1 and AFG2, respectively. Additionally, the half-life times for AFG1 and AFG2 photodegradation were found to be 11.95 and 11.55 min, respectively. Catalyst reuse investigations demonstrated that the composite could be reused at least 5 times without significant loss of efficacy. These findings highlight the effectiveness of the Bimetallic MIL-53 (Al, Ni)/ZnO NPs composite as a stable and efficient photocatalyst for the removal of AFG1 and AFG2 under mild conditions, showcasing its potential for practical applications in environmental remediation processes.

Keywords Aflatoxins, Photodegradtion process, Bimetallic MIL-53 (Al, Ni), Zinc oxide nanoparticles, Central composite design

Aflatoxins are secondary metabolites primarily produced by Aspergillus flavus and Aspergillus parasiticus fungi, naturally occurring in soil, grains, and various food crops[1,2]. These toxins are potent carcinogens and mutagens, posing significant health risks to humans and animals[3,4]. Furthermore, aflatoxins have detrimental environmental impacts due to their persistence and capacity for bioaccumulation, leading to soil and water contamination[5]. The consumption of aflatoxin-contaminated crops by animals results in bioaccumulation and subsequent environmental pollution through their waste products[6,7]. Aflatoxins can cause acute aflatoxicosis, leading to symptoms like vomiting, abdominal pain, and liver damage, and chronic exposure may lead to liver cancer, immune suppression, growth retardation, and adverse birth outcomes[1,8]. Livestock consuming aflatoxin-contaminated feed suffer from reduced growth rates, decreased milk production, immune system suppression, and liver damage[9,10]. The significance of aflatoxins in public health and environmental sustainability necessitates effective mitigation strategies, such as the photodegradation method, which has emerged as a promising approach for their removal[11–13].

Photodegradation, a novel approach utilizing light energy to degrade aflatoxins, has emerged as a promising method for their elimination[14–17]. Photodegradation is a process that involves the degradation of compounds through the absorption of light energy, typically ultraviolet (UV) light[11,18–23]. In the context of aflatoxins, exposure to UV light triggers chemical reactions that break down the toxin molecules into less harmful byproducts[24–27]. This mechanism offers a non-invasive and environmentally friendly means of aflatoxin removal without introducing additional chemical residues[28,29]. The significance of photodegradation lies in its high

Department of Chemistry, Payame Noor University, Tehran, Iran. ✉email: Z.Gordi@pnu.ac.ir

efficiency and specificity towards aflatoxins[30]. By targeting the toxin molecules directly, photodegradation can effectively reduce aflatoxin levels in contaminated food and feed products[31]. Moreover, this method offers a rapid and scalable approach to toxin removal, making it suitable for industrial applications where large volumes of contaminated materials need to be treated. The important advantages of the photodegradation process for reducing aflatoxin levels include high efficiency, environmental friendliness, preservation of nutritional quality, and proper degradation time[32].

Zinc oxide nanoparticles (ZnO NPs) have gained significant attention in recent years due to their unique properties and potential applications in various fields, including photocatalysis[33–36]. ZnO NPs have been extensively studied as photocatalysts for the degradation of organic pollutants, as they exhibit excellent photocatalytic activity under UV light irradiation[37,38]. One of the major challenges in photocatalysis is the efficient utilization of the photocatalyst and the enhancement of its photocatalytic activity[39]. Metal–organic frameworks (MOFs) have emerged as promising materials for enhancing the performance of photocatalysts due to their tunable structure, high surface area, and unique properties[40–42]. MOFs are a class of porous materials composed of metal nodes connected by organic linkers, which can be easily tailored to incorporate different metal ions and functional groups[18,41,43].

The combination of ZnO NPs and MOFs in a composite material offers several advantages for photocatalytic applications. ZnO NPs can act as the photocatalytic agent, while the MOF can provide a stable support structure and enhance the overall performance of the composite. The high surface area and porosity of MOFs can facilitate the adsorption of aflatoxins onto the composite material, increasing the efficiency of the photocatalytic degradation process[44–46]. Furthermore, the unique properties of MOFs, such as their tunable structure and surface chemistry, can be exploited to enhance the photocatalytic activity of ZnO NPs[47]. By incorporating specific functional groups or metal ions into the MOF structure, the composite material can exhibit enhanced catalytic properties, such as improved light absorption, charge separation, and electron transfer kinetics[48].

However, the practical application of many existing photocatalytic systems is hindered by their limited efficiency in degrading AFs, necessitating protracted reaction times or elevated catalyst loadings[49,50]. Furthermore, concerns persist regarding the long-term operational stability of some photocatalysts, which are susceptible to photocorrosion or deactivation during extended use[51,52], resulting in long degradation time to achieve to suitable degradation of AFG1 and AFG2. While various photocatalytic approaches have been explored for aflatoxin degradation, this research introduces a novel, highly efficient photocatalyst: a bimetallic MIL-53 (Al, Ni)/ZnO nanoparticle composite. Previous studies have investigated individual components (ZnO, MIL-53) or different bimetallic combinations for aflatoxin removal, but the synergistic combination of a bimetallic MIL-53(Al, Ni) with ZnO nanoparticles, optimized via a Box-Behnken design to maximize performance, represents a significant innovation. The use of a bimetallic MOF composite is expected to enhance the catalytic activity for AFG1 and AFG2 photodegradation due to the synergistic effect between the two metal centers[53]. The incorporation of two different metals into the MOF framework may enhance the overall stability of the composite material, preventing deactivation during the photocatalytic reaction[54,55]. This study's comprehensive approach, combining material synthesis, process optimization (identifying optimal pH, catalyst dosage, aflatoxin concentration, and H_2O_2 concentration), kinetic modeling, and reusability assessment, provides a more complete understanding of the catalyst's efficacy and potential for practical application. Unlike previous studies that may have focused on only one aspect (e.g., synthesis or kinetic analysis), this work presents a holistic evaluation of the Bimetallic MIL-53 (Al, Ni)/ZnO NP composite as a sustainable solution for aflatoxin remediation. The resulting high removal efficiencies, rapid degradation kinetics, and reusability demonstrate the superiority and practical applicability of this novel photocatalyst.

The United Nations Sustainable Development Goals (UNSDGs) represent a global call to action to end poverty, protect the planet, and ensure that all people enjoy peace and prosperity by 2030. This research directly addresses SDG 6: Clean Water and Sanitation by developing a novel Ni/Fe-MIL-53@ZnO nanocomposite for the efficient degradation of AFG1 and AFG2 in water. Aflatoxin contamination of water resources poses a significant threat to human health, particularly in regions where access to advanced water treatment is limited. This work contributes to ensuring the availability and sustainable management of water and sanitation for all. Furthermore, the reduction of aflatoxins also aligns with SDG 3: Good Health and Well-being, as these toxins are potent carcinogens, and their removal can significantly reduce the risk of related diseases. Finally, by focusing on photocatalytic degradation, this research moves toward more sustainable water purification technologies, supporting the broader aims of the UNSDGs.

Experimental

Materials and instruments

Aflatoxins, specifically AFG1 and AFG2, along with other compounds used in the preparation of the catalyst composite, such as zinc nitrate hexahydrate (≥99.0%), aluminum nitrate nonahydrate (≥98%), nickel (II) chloride hexahydrate (≥98%), sodium hydroxide(≥97.0%), and terephthalic acid (98%), were procured from Sigma-Aldrich (USA). All organic solvents, including methanol (HPLC grade, ≥99.9%), acetonitrile (HPLC grade, ≥99.9%), and dimethylformamide (DMF, ≥99.8%), were sourced from Merck (Germany).

AFG1 and AFG2 were quantified using a high-performance liquid chromatography (Knauer, Germany) method employing a photoreactor (UVE, LC tech) and an RF-20A fluorescence detector. The fluorescence detector was set to specific emission and excitation wavelengths of 435 nm and 362 nm, respectively, for AFG1 and AFG2 determination. Separation of the AFG1 and AFG2 was achieved using a Eurospher 100/5C18 column (4.6 mm ID, 5 µm ODS, 25 cm L). The Eurospher 100/5C18 column features a unpolar silica gel with a monomeric C18 (Octadecyl) modification. It is endcapped and has a carbon content of 16%. The column operates effectively at temperatures up to 40 °C, with a short-term tolerance of up to 50 °C, and boasts a specific surface area of 350 m2/g. The mobile phase consisted of a mixture of methanol/acetonitrile (50:50 v/v) and phosphate

buffer (0.05 mM, pH 4), with a ratio of 40:60 v/v and a flow rate of 1.0 mL min^{-1}[47]. The structural analysis of the catalyst composite included investigations using Fourier-Transform Infrared Spectroscopy (FT-IR) on a Bruker instrument (Germany), X-ray Diffraction Spectroscopy (XRD) on a Bruker D8 ADVANCE instrument (Germany), BET analysis using BELSORP Mini II (MicrotracBEL Corp, Japan), and Field Emission-Scanning Electron Microscopy (FE-SEM) with a Mira 3 Tescan instrument (Czech Republic). Sample pH adjustments were conducted using a pH meter (Metrohm 780, Herisau, Switzerland) during the degradation process.

Photocatalyst synthesis

ZnO nanoparticles

A hydrothermal method was employed to synthesize ZnO NPs following a previously published protocol[56]. In this procedure, 0.237 g of $Zn(NO_3)_2{\cdot}6H_2O$ was dissolved in 25 mL of distilled water by stirring. Subsequently, a 5.0 M sodium hydroxide solution was slowly added dropwise until the pH of the solution reached approximately 12. The resulting mixture was then transferred to an autoclave and heated at 150 °C for 2 h. After cooling to room temperature, the precipitate was separated, washed with distilled water, and dried in an oven at 80 °C for 12 h.

Bimetallic MIL-53 (Al, Ni)/ZnO NPs

Bimetallic MIL-53 (Al, Ni) was synthesized using a hydrothermal method that closely followed the procedure outlined in a previous study[53]. For this purpose, a mixture of ZnO NPs (0.5 g), $NiCl_2{\cdot}6H_2O$ (0.547g), $Al(NO_3)_3{\cdot}9H_2O$ (0.864 g), and terephthalic acid (2.49 g) were poured in 40 mL of DMF, followed by sonicating for 20 min. The resulting mixture was then transferred to an autoclave and heated at 150 °C for 14 h. Upon cooling to room temperature, the precipitate (Bimetallic MIL-53 (Al, Ni)/ZnO NPs) was isolated, washed with distilled water, and dried in an oven at 80 °C for 12 h. Additionally, to assess the photocatalytic performance, Bimetallic MIL-53 (Al, Ni) was also prepared using the same method described above, but without adding ZnO NPs. The schematic representation for the synthesis of the Bimetallic MIL-53 (Al, Ni)/ZnO NPs is presented in Fig. 1.

Photodegradation process

The experiment utilized an initial AF concentration of 35 mg L^{-1}, 109 mg of Bimetallic MIL-53 (Al, Ni)/ZnO NPs as the photocatalyst, and a sample solution volume of 100 mL to degrade the aflatoxins (AFs). The final concentration of the photocatalyst in the solution was 1.09 g L^{-1}). A hydrochloric acid solution with a concentration of 0.1 mol L^{-1} was used to adjust the pH of the sample solution to 4.1 before introducing the photocatalyst. The resulting mixture was gently shaken for 30 min at a rate of 200 rpm to establish an equilibrium state of adsorption of AFG1 and AFG2 on the photocatalyst, without exposure to UV light. After adding hydrogen peroxide (3 mM), the mixture was agitated at 150 rpm under UVC lamp (36 W, FPL, 4 pins, Mazda, Japan) exposure for 60 min at a distance of 15 cm from the solution surface. Bimetallic MIL-53 (Al, Ni)/ZnO NPs were then separated from the mixture using a centrifuge, and the AF concentration in the supernatant was determined using the HPLC method. The percentage of removal (R%) was calculated using the following equation:

$$R\% = \frac{C_i - C_f}{C_i} * 100 \quad (1)$$

where C_f and C_i represent the IMB concentration at time (t) and its initial concentration (t = o min).

Results and discussion

Photocatalyst characterization

The FE-SEM images in Fig. 2 depict the Bimetallic MIL-53 (Al, Ni) and the Bimetallic MIL-53 (Al, Ni)/ZnO NPs composite. Figure 2a reveals the prismatic structure of Bimetallic MIL-53 (Al, Ni) particles, exhibiting irregular formations with varying sizes. The particles exhibit diverse shapes within their texture, showcasing a non-

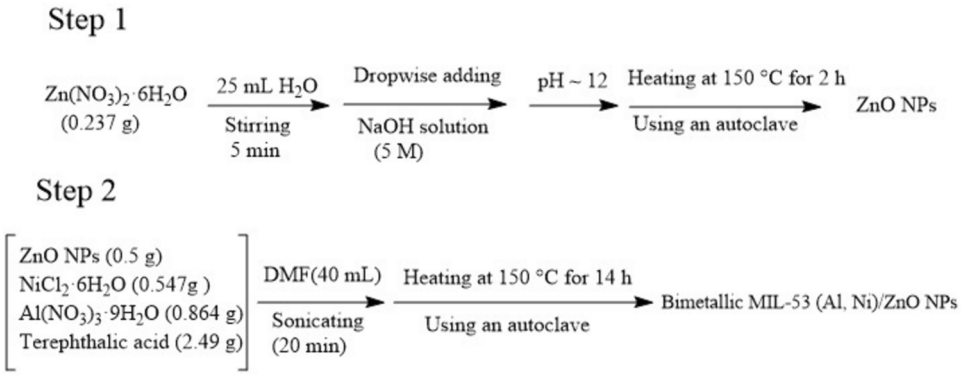

Fig. 1. The schematic representation for the synthesis of the Bimetallic MIL-53 (Al, Ni)/ZnO NPs as a photocatalyst.

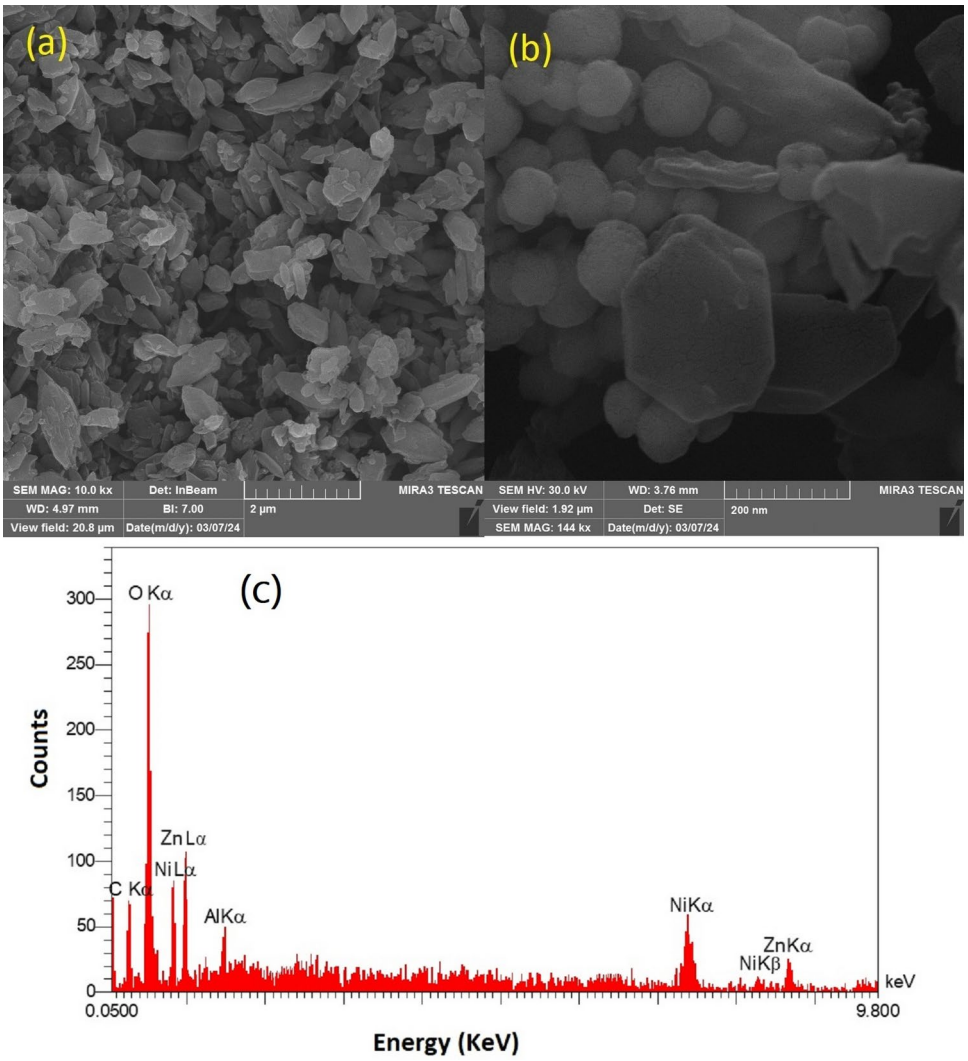

Fig. 2. The FE-SEM image of the Bimetallic MIL-53 (Al, Ni) (**a**) and the Bimetallic MIL-53 (Al, Ni)/ZnO NPs composite (**b**), and the EDX pattern of the Bimetallic MIL-53 (Al, Ni)/ZnO NPs composite (**c**).

uniform structure. The dimensions of the Bimetallic MIL-53 (Al, Ni) particles range from approximately 200 nm to 5 µm in length and 100 nm to 2 µm in width. In Fig. 2b, spherical ZnO NPs are observed to be adhering to the Bimetallic MIL-53 (Al, Ni) particles, displaying smaller dimensions. The ZnO NPs typically measure less than 100 nm in size, with variations noted within the range of 40 to 120 nm. This composite structure highlights the between Bimetallic MIL-53 (Al, Ni) and ZnO NPs, showcasing a promising platform for the photodegradation active of AFG1 and AFG2.

The Energy Dispersive X-ray Spectroscopy (EDX) pattern of the Bimetallic MIL-53 (Al, Ni)/ZnO NPs composite is presented in Fig. 2c. The composite material was found to consist of carbon, oxygen, nickel, aluminum, and zinc, with weight percentages of 55.23%, 18.62%, 5.75%, 4.12%, and 16.28%, respectively. This elemental composition confirms the presence of the intended components within the composite. Moreover, a comprehensive analysis of the EDX pattern revealed no additional peaks beyond those corresponding to the expected elements. This observation indicates the high purity of the synthetic composite, with no discernible impurities or foreign elements present in its structure.

The FTIR spectra of the Bimetallic MIL-53 (Al, Ni) and the Bimetallic MIL-53 (Al, Ni)/ZnO NPs composite are illustrated in Fig. 3. The prominent peaks at 3371 cm^{-1} and 3402 cm^{-1} correspond to the stretching vibrations of O–H groups in Bimetallic MIL-53 (Al, Ni) and the Bimetallic MIL-53 (Al, Ni)/ZnO NPs composite, respectively. Furthermore, the stretching vibration of the C = O group in Bimetallic MIL-53 (Al, Ni) is identified at 1705 cm^{-1}, exhibiting a shift to 1682 cm^{-1} in the Bimetallic MIL-53 (Al, Ni)/ZnO NPs composite. This shift is attributed to the presence of unreacted COOH groups in terephthalic acid. The peak at 1388 cm^{-1} corresponds to the symmetric stretching of COO^- groups in both Bimetallic MIL-53 (Al, Ni) and the Bimetallic MIL-53 (Al, Ni)/ZnO NPs composite, indicating the interaction between Al or Ni ions with terephthalic acid leading to the formation of Bimetallic MIL-53 (Al, Ni). Moreover, the peak at 640 cm^{-1}, associated with Al-O bonds in Bimetallic MIL-53 (Al, Ni), shifts to 617 cm^{-1} in the Bimetallic MIL-53 (Al, Ni)/ZnO NPs composite.

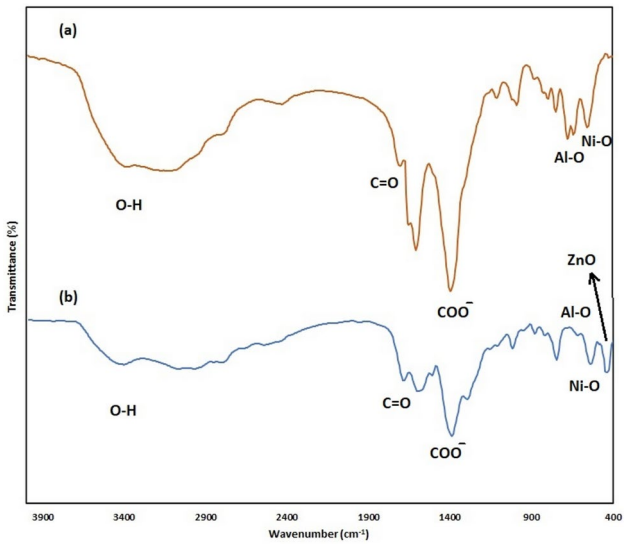

Fig. 3. The FTIR spectra of the Bimetallic MIL-53 (Al, Ni) (**a**) and the Bimetallic MIL-53 (Al, Ni)/ZnO NPs composite (**b**).

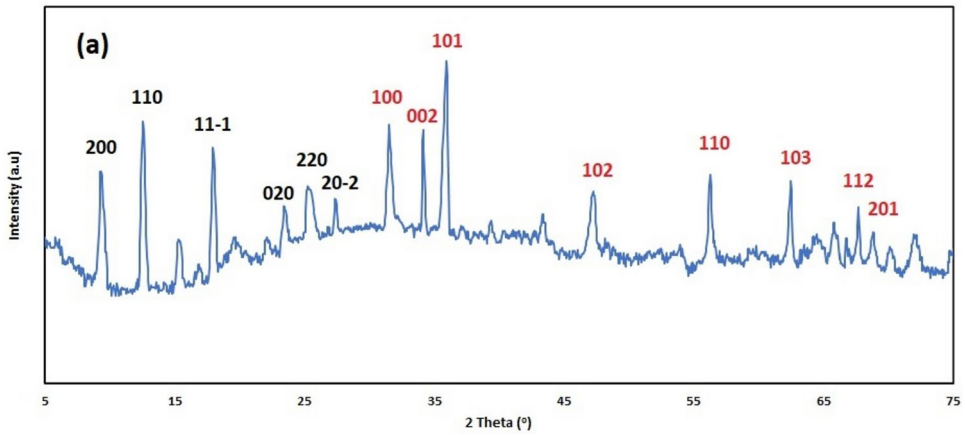

Fig. 4. The XRD patterns of the Bimetallic MIL-53 (Al, Ni)/ZnO NPs composite.

Additionally, peaks at 555 cm^{-1} and 532 cm^{-1} can be attributed to Fe–O bonds in the Bimetallic MIL-53 (Al, Ni) and the Bimetallic MIL-53 (Al, Ni)/ZnO NPs composite, respectively. Interestingly, the presence of a peak at 432 cm^{-1} indicates the characteristic signature of ZnO in the Bimetallic MIL-53 (Al, Ni)/ZnO NPs composite, underscoring the successful incorporation of ZnO NPs into the composite structure.

The X-ray diffraction (XRD) pattern of the Bimetallic MIL-53 (Al, Ni)/ZnO NPs composite is illustrated in Fig. 4. The peaks corresponding to 2 theta values of 9.4°, 12.9°, 17.9°, 23.5°, 25.3°, and 27.3° are attributed to MIL-53, with diffraction planes identified as 200, 110, 11–1, 020, 220, and 20–2, respectively[57], respectively. Additionally, the presence of ZnO NPs within the composite is confirmed by peaks observed at 31.5°, 34.2°, 36.0°, 47.3°, 56.3°, 62.5°, 67.7°, and 68.9°, corresponding to the crystallographic planes 100, 002, 101, 102, 110, 103, 112, and 201, respectively [56].

The results of the BET analysis for the Bimetallic MIL-53 (Al, Ni)/ZnO NPs composite indicate that the composite exhibits a surface area of 4.5761 m2 $g^{-}1$, with a mean pore diameter of 5.8361 nm. The total pore volume at a relative pressure of 0.990 is measured at 0.011342 cm3 $g^{-}1$, and the specific microporous surface area is determined to be 1.0361 cm3(STP) $g^{-}1$. These findings suggest that the composite material possesses a well-defined porous structure with significant surface area, which could be advantageous for the adsorption of AFG1 and AFG2 before their photodegradation as the catalyst under UV exposure (Fig. 5a).

The Transmission Electron Microscopy (TEM) image of the bimetallic MIL-53 (Al, Ni)/ZnO NPs composite is presented in Fig. 5b. The analysis reveals that the bimetallic MIL-53 (Al, Ni) particles exhibit a prismatic morphology, with dimensions measuring approximately 250 nm in width and 75 nm in length. Conversely, the ZnO NPs are observed to possess a spherical shape, with a diameter of approximately 90 nm. These morphological

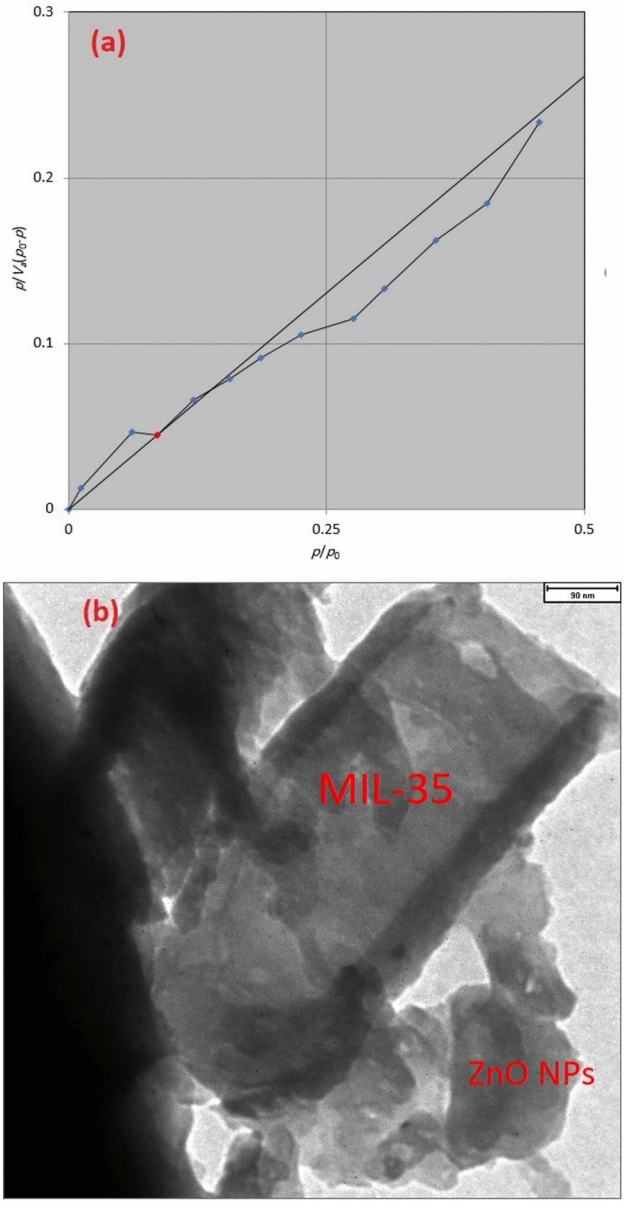

Fig. 5. The BET analysis (**a**) and TEM image (**b**) of the Bimetallic MIL-53 (Al, Ni).

characteristics are consistent with the findings from FESEM, which further corroborates the structural integrity and size distribution of the synthesized materials.

Optimization of the degradation procedure

Type of photocatalyst and lamp source

The type of photocatalyst plays a crucial role in the degradation of pollutants through photocatalysis. Photocatalyst properties such as surface area, band gap energy, and morphology can significantly impact their efficiency in degrading pollutants. Adding a compound into the photocatalyst structure to form hybrid materials can modify its electronic band structure and enhance its photocatalytic performance. These modifications can improve light absorption and charge separation, leading to increased efficiency in pollutant degradation. In this study, the activity of several photocatalysts, including ZnO NPs, Bimetallic MIL-53 (Al, Ni), and Bimetallic MIL-53 (Al, Ni)/ZnO NPs, in the presence or absence of H_2O_2 for the degradation for degrading AFG1 and AFG2 was compared[58]. For this procedure, 50 mg of each photocatalyst was added to a sample solution (100 mL) containing AFG1 and AFG2 (25 mg L^{-1}), and the pH was adjusted to 5. The mixture was shaken for 30 min before adding H_2O_2 (2 mM) and exposing it to UV light, followed by further shaking for 60 min. The photocatalyst was separated, and the AF concentration was determined using the HPLC method to calculate R%. Each experiment was performed in triplicate under the same conditions to calculate the mean of R% and standard deviation (Table 1). In all samples, the R% of AFG1 and AFG2 should be improved by adding H_2O_2 with a concentration of 2 mM, showing that the presence of this compound can increase the formation of free radicals in the solution,

Contaminant	R% ± SD[1]				
	H_2O_2 concentration (mM)	Without catalyst	Bimetallic MIL-53 (Al, Ni)	ZnO NPs	Bimetallic MIL-53 (Al, Ni)/ZnO NPs
AF G1	0.0	3.16 ± 0.92	23.77 ± 1.21	63.44 ± 1.97	74.89 ± 1.81
	2.0	8.46 ± 0.89	25.53 ± 1.16	69.71 ± 1.83	78.29 ± 1.87
AF G2	0.0	3.78 ± 0.96	22.81 ± 1.33	64.29 ± 1.75	74.52 ± 1.96
	2.0	9.82 ± 0.84	27.44 ± 1.29	68.09 ± 1.67	79.36 ± 1.92

Table 1. Effect of photocatalyst type on the removal of AFs. [1]Removal percentage ± Standard deviation.

Photocatalyst component	Amount (g)	R%	
		AFG1	AFG2
$NiCl_2{\cdot}6H_2O$	0.274	69.48	67.54
$Al(NO_3)_3{\cdot}9H_2O$	0.432		
$NiCl_2{\cdot}6H_2O$	0.547	78.31	79.36
$Al(NO_3)_3{\cdot}9H_2O$	0.864		
$NiCl_2{\cdot}6H_2O$	0.820	76.25	75.49
$Al(NO_3)_3{\cdot}9H_2O$	1.296		
$NiCl_2{\cdot}6H_2O$	1.094	75.32	75.18
$Al(NO_3)_3{\cdot}9H_2O$	1.728		

Table 2. Optimization of the photocatalyst component amount in the presence of a constant amount of ZnO NPs (0.5 g) and terephthalic acid (2.49 g).

as a result; the R% of AFG1 and AFG2 was improved. The absence of a photocatalyst resulted in the lowest R% value, indicating the significant impact of photocatalysts on the degradation efficiency. Among the tested photocatalysts, Bimetallic MIL-53 (Al, Ni) exhibited low activity in degrading AFG1 and AFG2, while ZnO NPs demonstrated moderate efficacy under specific conditions. However, the composite formed by combining Bimetallic MIL-53 (Al, Ni) with ZnO NPs showed the highest R% value, suggesting that although Bimetallic MIL-53 (Al, Ni) alone had limited photocatalytic activity, its presence in the Bimetallic MIL-53 (Al, Ni)/ZnO NPs composite enhanced the photocatalytic performance of ZnO NPs through the promotion of synergistic effects. This enhancement may be attributed to the potential role of Bimetallic MIL-53 (Al, Ni) as a co-catalyst with ZnO NPs, facilitating efficient charge separation and transfer processes during photocatalysis. Therefore, the Bimetallic MIL-53 (Al, Ni)/ZnO NPs composite was selected as the photocatalyst for further study.

Visible light-driven photocatalysis has emerged as a promising technology for environmental remediation due to its potential for utilizing solar energy, thereby reducing energy costs. However, there is still challange to find the materials with good efficiency for degradation AFG1 and AFG2. We used a visible light lamp to degrade AFG1 and AFG2 and did not get good results, so a UV source was used for the degradation procedure.

The optimizatiSon of the ratio of photocatalyst components

Several photocatalysts were synthesized by systematically mixing three components: ZnO NPs, $NiCl_2{\cdot}6H_2O$, and $Al(NO_3)_3{\cdot}9H_2O$ in varying proportions. Specifically, a molar ratio of 2:1 was maintained between $NiCl_2{\cdot}6H_2O$ and $Al(NO_3)_3{\cdot}9H_2O$, while a fixed quantity of 0.5 g of ZnO NPs and 2.49 g of terephthalic acid were included in all formulations. The results, presented in Table 2, demonstrate that the R% of AFG1 and AFG2 initially increased with the addition of $NiCl_2{\cdot}6H_2O$, reaching a maximum at 0.547 g, and with $Al(NO_3)_3{\cdot}9H_2O$, peaking at 0.864 g. Beyond these optimal concentrations, further increases in the amounts of these salts resulted in a slight reduction in R%, indicating that excess quantities do not enhance, and may even hinder photocatalytic performance. In line with the principles of green chemistry aimed at minimizing chemical use and enhancing efficiency, the lowest effective amounts of $NiCl_2{\cdot}6H_2O$ (0.547 g) and $Al(NO_3)_3{\cdot}9H_2O$ (0.864 g) were determined to be optimal for maximizing the photocatalytic degradation of AFG1 and AFG2.

Optimization of other factors

Central composite design (CCD) is a powerful experimental design technique that can be used to optimize complex processes such as photodegradation procedures[14]. By systematically varying the levels of each factor and replicating experiments at the center point, CCD can help researchers understand the interactions between factors and identify optimal conditions for maximum degradation efficiency. One of the main advantages of CCD is its ability to balance the trade-off between exploring the design space comprehensively and minimizing the number of experimental runs required. This makes it an efficient tool for optimizing processes like photodegradation, which can be time-consuming and costly to investigate.

Furthermore, CCD also allows researchers to evaluate the curvature of the response surface, which can help them identify optimal operating conditions more accurately. Factors such as pH, AF concentration, temperature, catalyst amount, and H_2O_2 concentration can significantly impact the degradation rate. To illustrate the use of

CCD in optimizing photodegradation procedures, Table 3 presents the levels of these factors and the generated design for the optimization of AF degradation.

By using CCD, researchers can efficiently explore the effects of these factors and their interactions, leading to the development of a predictive model that guides the selection of optimal conditions for maximum degradation efficiency. Each run is typically performed in triplicate, and the response is calculated from the mean of the results. The responses are then analyzed using ANOVA at a confidence interval of 95%, with a theoretical p-value of 0.05 (Table 4)[59].

In the case of AF degradation, the results indicated that four factors significantly impact removing both AFs due to the p-value of each factor being lower than 0.05. In addition, the binary interaction between pH and catalyst amount is significant for removing both AFs. Furthermore, the binary interaction between pH and H_2O_2 concentration for the removal of AFG1 and the binary interaction between AF concentration and H_2O_2 concentration for the removal of AFG2 have a meaningful effect. Other binary interactions have a non-significant impact on removing both AFs.

The presented models for removing both AFs are significant, and the obtained quadratic equations of the models are as follows:

$$\begin{aligned} &\mathrm{R\%forAFG1} = 91.9268 - 6.82889 * \mathrm{A} + 5.33444 * \mathrm{B} + 2.04889 * \mathrm{C} + 1.95111 * \mathrm{D} + 4.0275 * \\ &\mathrm{AB} + 0.7025 * \mathrm{AC} + 1.9375 * \mathrm{AD} + 0.8125 * \mathrm{BC} - 0.4425 * \mathrm{BD} - 1.4375 * \mathrm{CD} - 0.327018 * \\ &\mathrm{A}^2 - 8.82702 * \mathrm{B}^2 - 4.82702 * \mathrm{C}^2 - 2.32702 * \mathrm{D}^2 \end{aligned} \quad (2)$$

Factor	Name	Units	Minimum	Maximum	Mean	Std. Dev	
A	pH	--	4.00	7.00	5.50	1.18	
B	Catalyst amount	mg	50.00	150.00	100.00	39.39	
C	AF concentration	mg/L	20.00	40.00	30.00	7.88	
D	H_2O_2 concentration	mM	1.0000	5.00	3.00	1.58	
Std	**Run**	**A**	**B**	**C**	**D**	**AFG1**	**AFG2**
23	1	0	0	0	−1	86.11	88.5
24	2	0	0	0	1	88.79	88.8
17	3	−1	0	0	0	92.89	96.03
3	4	−1	1	−1	−1	81.71	81.98
25	5	0	0	0	0	96.45	95.65
11	6	−1	1	−1	1	82.13	84.26
5	7	−1	−1	1	−1	81.39	86.78
6	8	1	−1	1	−1	59.11	65.96
4	9	1	1	−1	−1	68.23	72.28
7	10	−1	1	1	−1	88.75	87.3
26	11	0	0	0	0	97.16	93.72
12	12	1	1	−1	1	81.65	79.56
18	13	1	0	0	0	86.01	87.27
13	14	−1	−1	1	1	82.33	86.1
14	15	1	−1	1	1	64.05	69.28
22	16	0	0	1	0	87.61	89.81
1	17	−1	−1	−1	−1	80.35	81.46
21	18	0	0	−1	0	82.29	85.49
9	19	−1	−1	−1	1	83.29	81.78
28	20	0	0	0	0	92.03	94.21
2	21	1	−1	−1	−1	51.51	57.64
16	22	1	1	1	1	82.25	81.88
15	23	−1	1	1	1	85.17	87.58
8	24	1	1	1	−1	79.83	83.6
30	25	0	0	0	0	90.89	94.57
27	26	0	0	0	0	93.11	92.39
29	27	0	0	0	0	94.82	95.53
19	28	0	−1	0	0	75.56	79.87
10	29	1	−1	−1	1	62.45	67.96
20	30	0	1	0	0	86.34	86.43

Table 3. Factors, levels, and central composite design for the removal of AFs.

Source	df	AFG1					AFG2				
		Sum of Squares	Mean Square	F-value	p-value	Significant	Sum of Squares	Mean Square	F-value	p-value	Significant
Model	14	3466.39	247.60	26.22	< 0.0001	+	2546.75	181.91	40.55	< 0.0001	+
A	1	839.41	839.41	88.88	< 0.0001	+	646.08	646.08	144.01	< 0.0001	+
B	1	512.21	512.21	54.23	< 0.0001	+	257.19	257.19	57.33	< 0.0001	+
C	1	75.56	75.56	8.00	0.0127	+	116.94	116.94	26.07	0.0001	+
D	1	68.52	68.52	7.26	0.0167	+	26.16	26.16	5.83	0.0290	+
AB	1	259.53	259.53	27.48	< 0.0001	+	165.64	165.64	36.92	< 0.0001	+
AC	1	7.90	7.90	0.8360	0.3750	-	1.56	1.56	0.3483	0.5639	-
AD	1	60.06	60.06	6.36	0.0235	+	18.06	18.06	4.03	0.0632	-
BC	1	10.56	10.56	1.12	0.3070	-	0.5625	0.5625	0.1254	0.7282	-
BD	1	3.13	3.13	0.3317	0.5732	-	1.66	1.66	0.3709	0.5516	-
CD	1	33.06	33.06	3.50	0.0810	-	22.56	22.56	5.03	0.0405	+
A^2	1	0.2771	0.2771	0.0293	0.8663	-	0.1295	0.1295	0.0289	0.8673	-
B^2	1	201.87	201.87	21.37	0.0003	+	177.47	177.47	39.56	< 0.0001	+
C^2	1	60.37	60.37	6.39	0.0232	+	36.95	36.95	8.24	0.0117	+
D^2	1	14.03	14.03	1.49	0.2417	-	19.97	19.97	4.45	0.0521	-
Residual	15	141.67	9.44				67.30	4.49			
Lack of Fit	10	110.70	11.07	1.79	0.2708	-	59.91	5.99	4.05	0.0679	-
Pure Error	5	30.97	6.19				7.39	1.48			
Cor Total	29	3608.06					2614.05				

Table 4. One-Way ANOVA analysis for assessing factor significance.

AFG1				AFG2			
Std. Dev	**3.07**	**R^2**	**0.9607**	**Std. Dev**	**2.12**	**R^2**	**0.9743**
Mean	82.14	**Adjusted R^2**	0.9241	**Mean**	84.12	**Adjusted R^2**	0.9502
C.V. %	3.74	**Predicted R^2**	0.8646	**C.V. %**	2.52	**Predicted R^2**	0.8823
		Adeq Precision	21.4939			**Adeq Precision**	26.8810

Table 5. Statistical parameters for the fitted equations.

$$\begin{aligned} R\%\text{for}AFG2 = {} & 92.8857 - 5.99111 * A + 3.78 * B + 2.54889 * C + 1.20556 * D + 3.2175 * \\ & AB + 0.3125 * AC + 1.0625 * AD + 0.1875 * BC - 0.3225 * BD - 1.1875 * CD + 0.223596 * \\ & A^2 - 8.2764 * B^2 - 3.7764 * C^2 - 2.7764 * D^2 \end{aligned} \quad (3)$$

The fit of the equations was assessed by examining the R-squared (R^2) and adjusted R-squared values. The obtained R^2 values were 0.9607 and 0.9743, while the adjusted R^2 values were 0.9241 and 0.9502 for the removal of AFG1 and AFG2, respectively. These values indicate a strong fit of the equations with the experimental data. Moreover, the predicted R^2 values for the removal of AFG1 and AFG2 were 0.8646 and 0.8823, demonstrating the models' ability to accurately predict the removal efficiencies for both AFG1 and AFG2 (Table 5).

The negative coefficient of pH in the developed equations suggests that an increase in pH leads to a decrease in the degradation percentage of both AFs. Therefore, the degradation process is more effective in acidic conditions in the presence of hydronium ions. Additionally, higher H_2O_2 concentration and increased amounts of photocatalyst positively influence the degradation process of AFG1 and AFG2, leading to higher removal percentages. The increased H_2O_2 concentration enhances the generation of free radicals in the solution, thereby improving degradation efficiency. Similarly, greater amounts of photocatalyst enhance light absorption, resulting in increased electron–hole pair formation and improved degradation efficiency. The results indicated that increasing the initial concentration of AFG1 and AFG2 initially led to a higher decomposition rate, but beyond a certain threshold (35 mgL^{-1}), the rate decreased. This phenomenon can be explained by at low concentrations, the number of AFG1 and AFG2 molecules is the limiting factor. As the concentration increases, more molecules are available for reaction, leading to a higher rate. However, at high concentrations, the available active sites on the catalyst surface become saturated, limiting the decomposition rate. Furthermore, high concentrations of AFG1 and AFG2 may reduce the penetration of UV light into the solution, decreasing the efficiency of photocatalysis.

The interactions between the factors affecting the degradation of both AFs were visually represented in Fig. 6. The figures illustrate that simultaneous increases in photocatalyst amount and decreases in pH enhance the removal percentages of both AFs (Fig. 6a and c). Moreover, a simultaneous increase in H_2O_2 concentration and decrease in pH significantly improve the R% of AFG1 (Fig. 6b), while a similar trend is observed for AFG2 with a simultaneous increase in H_2O_2 and AFG2 concentration (Fig. 6d).

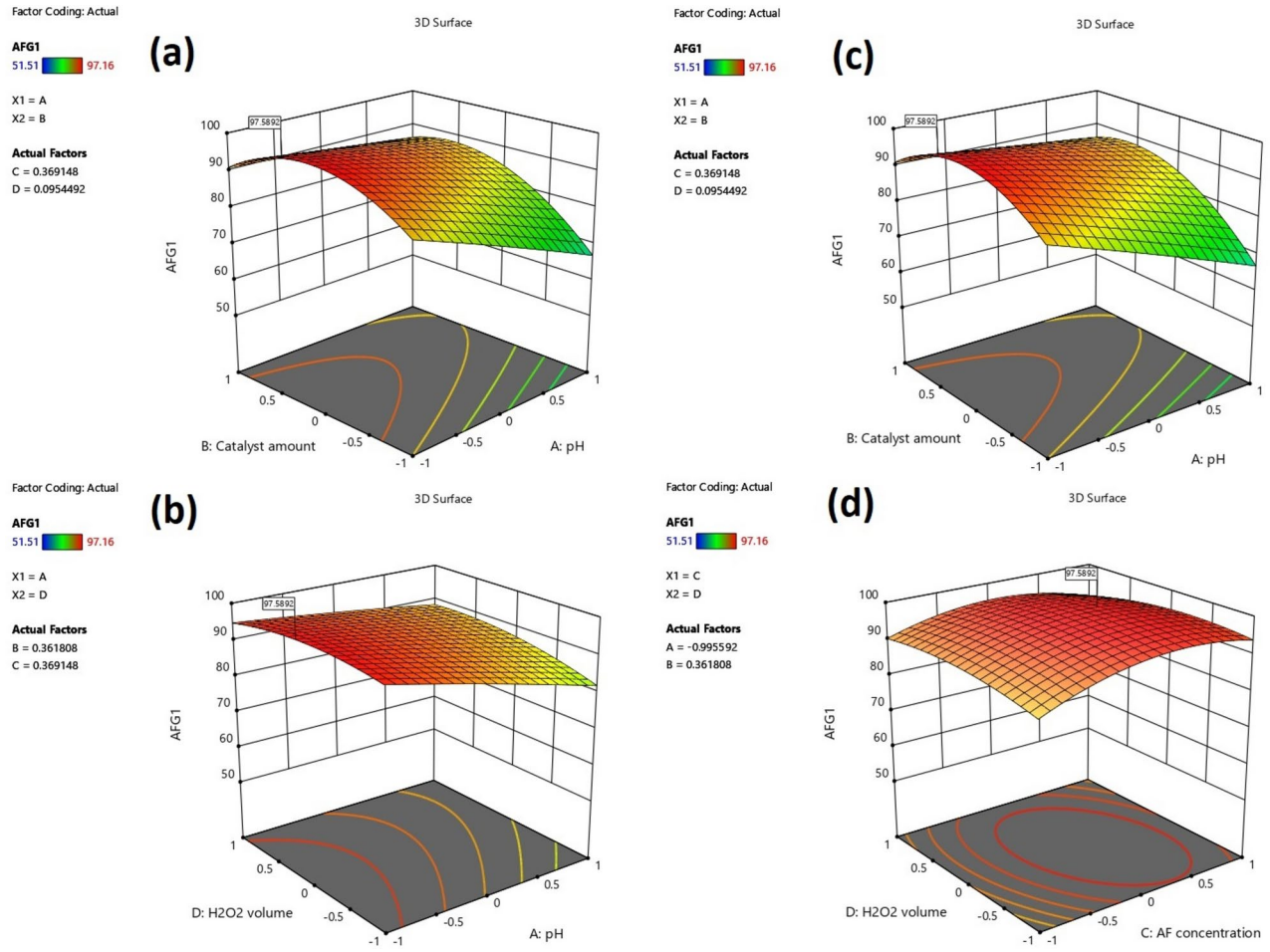

Fig. 6. The significant binary interactions among factors influencing the degradation of AFG1 and AFG2.

The developed models for both AFG1 and AFG2 were analyzed to determine the optimal values of the factors, resulting in pH 4.1, 109 mg of photocatalyst, 35 mgL^{-1} of AFs, and 3 mM of H_2O_2 concentration. Under these conditions, the predicted removal efficiencies for AFG1 and AFG2 were 97.43% and 98.69%, respectively.

Kinetic study

A pseudo-first-order model was selected and used to investigate the kinetic of the photodegradation procedure. The following equation is a nonlinear format of the model:

$$C_f = xe^{-kt} + E \tag{4}$$

In the equation, t (min), C_f (mg L^{-1}), x (mg L^{-1}), k(min^{-1}), and E are the degradation time, final concentration of AFG1 or AFG2, intional concentration of AFG1 or AFG2, rate constant, respectively. Besides, Eq. 5 was used to determine the half-life time ($t_{1/2}$) of the removal procedure:

$$t_{1/2} = \frac{0.693}{k} \tag{5}$$

The kinetics of AF degradation using the Bimetallic MIL-53 (Al, Ni)/ZnO NPs composite was investigated under optimized conditions as obtained in the previous step (Sect. 3.1.1). In this study, a photocatalyst weighing 109 mg was added to a solution with a pH adjusted to 4.1. The solution contained AFG1 and AFG2 at a concentration of 35 mg L^{-1}. The mixture was shaken for 30 min at a rate of 200 rpm to establish an equilibrium state of adsorption of AFG1 and AFG2 on the photocatalyst, without exposure to UV light. Hydrogen peroxide (3 mM) was then added, and the mixture was agitated at 150 rpm while being exposed to UV light for a duration of 0 to 60 min. Afterward, the Bimetallic MIL-53 (Al, Ni)/ZnO NPs composite was separated from the mixture using a centrifuge. The concentrations of AFG1 and AFG2 in the supernatant were determined using the HPLC method. The results are presented in Fig. 7 and Table 6. The obtained data fit well with the equations used to remove AFG1 and AFG2, as evidenced by the R-squared values of 0.98 and 0.99, respectively.

Furthermore, the photocatalytic process utilizing the Bimetallic MIL-53 (Al, Ni)/ZnO NPs composite as the catalyst demonstrated a favorable reaction rate, with pseudo-first-order rate constants of 0.058 ± 0.002 min^{-1} and

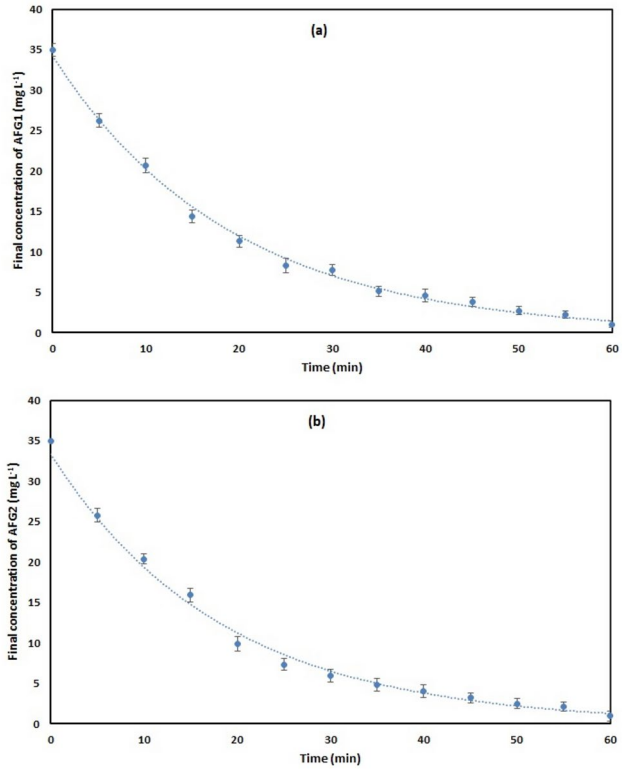

Fig. 7. The kinetics of AFG1 and AFG2 degradation using the Bimetallic MIL-53 (Al, Ni)/ZnO NPs composite.

Contaminant	R^2	k ± SD[1] (min^{-1})	x ± SD ($mg\ L^{-1}$)	E ± SD ($mg\ L^{-1}$)	$t_{1/2}$ (min)
AFG1	0.997	0.058 ± 0.002	34.182 ± 0.545	0.780 ± 0.435	11.95
AFG2	0.995	0.060 ± 0.003	34.630 ± 0.671	0.491 ± 0.517	11.55

Table 6. Kinetic studies for degradation of AFG1 and AFG2 using Bimetallic MIL-53 (Al, Ni)/ZnO NPs composite as a photocatalyst. [1]Standard Deviation.

$0.060 \pm 0.003\ min^{-1}$ for the removal of AFG1 and AFG2, respectively. The bandgap energies of ZnO NPs and the Bimetallic MIL-53 (Al, Ni)/ZnO NPs composite were measured using the Diffuse Reflectance Spectroscopy (DRS) method, yielding values of 3.35 eV and 3.16 eV, respectively. The incorporation of Bimetallic MIL-53 (Al, Ni) into the ZnO NPs resulted in a decreased bandgap, which suggests that the Bimetallic MIL-53 (Al, Ni)/ZnO NPs composite demonstrates enhanced photocatalytic activity for the degradation of AFG1 and AFG2 compared to the unmodified ZnO NPs. These results imply that the increased degradation rates of AFG1 and AFG2 can be attributed to the smaller bandgap energy of the Bimetallic MIL-53 (Al, Ni)/ZnO NPs composite. This reduced bandgap facilitates the absorption of a broader spectrum of UV wavelengths, leading to an enhanced generation of electron–hole pairs, which in turn drives the photocatalytic degradation process more effectively. Furthermore, the Bimetallic MIL-53 (Al, Ni)/ZnO NPs composite exhibits improved efficiency in separating electron–hole pairs, which minimizes the recombination rate, resulting in a more efficient photocatalytic reaction. Besides, the results indicate that the degradation process follows a predictable kinetic behavior, suggesting a strong correlation between the concentration of the pollutants and the reaction rate. The similarity in the rate constants for both aflatoxins implies that the bimetallic composite effectively interacts with both contaminants under the same experimental conditions, underscoring its broad-spectrum efficacy. The half-life times for the photodegradation of AFG1 and AFG2 were calculated using Eq. 5 to be 11.95 min and 11.55 min, respectively—further support the rapid degradation capabilities of the photocatalyst. A shorter half-life corresponds to a more efficient degradation process, which is crucial for practical applications, particularly in environmental remediation, where the aim is to reduce toxic pollutant concentrations in a timely manner. Therefore, the results strongly indicate that the Bimetallic MIL-53 (Al, Ni)/ZnO NPs composite serves as a highly effective photocatalyst for the simultaneous degradation of AFG1 and AFG2. Incorporating bimetallic components (Al and Ni) enhances the photocatalytic activity, possibly through improved charge separation and increased surface area, allowing for more active sites for the reaction.

Identifying the Reactive Oxygen Species (ROS) involved

To determine the predominant reactive oxygen species (ROS) responsible for the photocatalytic degradation of AFG1 and AFG2 using the Bimetallic MIL-53 (Al, Ni)/ZnO NPs as a catalyst, a series of scavenging experiments were conducted. This methodology utilized specific chemical scavengers that selectively neutralize individual ROS, thereby allowing for the assessment of their respective contributions to the degradation process. The selected scavengers included Benzoquinone (BQ), which effectively captures superoxide radicals ($\bullet O_2^-$), Isopropanol (IPA) known for scavenging hydroxyl radicals (•OH), and Ammonium Oxalate (AO), which targets the photogenerated holes (h^+).

The impact of these scavengers on the photocatalytic degradation of AFG1 and AFG2 was evaluated by introducing them into the reaction solution prior to irradiation. The results, illustrated in Fig. 8, demonstrate a significant decrease in the degradation rate upon the addition of IPA, indicating that •OH radicals play a pivotal role in the photocatalytic degradation of both AFG1 and AFG2. Conversely, the presence of AO or BQ did not notably alter the degradation rate, suggesting that the contributions of h^+ and $\bullet O2^-$ are minimal in this process. These findings strongly indicate that •OH radicals are the primary active species responsible for the effective degradation of AFG1 and AFG2 when using the Bimetallic MIL-53 (Al, Ni)/ZnO NPs composite. This conclusion aligns with the proposed degradation mechanism, in which photogenerated electrons from ZnO NPs react with molecular oxygen to form $\bullet O_2^-$, which then reacts with H^+ ions to produce •OH. In the presence of H_2O_2, hydroxide radical (•OH) and hydroxide anion (OH^-) are formed as a result of the reaction between H_2O_2 and produced electrons. This detailed investigation into the roles of various ROS provides crucial insights into the underlying mechanisms of photocatalytic degradation of AFG1 and AFG2 by the aforementioned composites. Furthermore, it underscores the significant role of •OH radicals in this process, highlighting the potential of these photocatalysts for effective environmental remediation of AFG1 and AFG2 contamination. The following equations summarize the proposed mechanism for the degradation of AFG1 and AFG2 utilizing the prepared photocatalysts:

(i) Photogenerated electrons.

$$\text{Bimetallic MIL-53 (Al, Ni)/ZnO NPs (VB)} + h\nu \rightarrow \text{Bimetallic MIL-53 (Al, Ni)/ZnO NPs (VB)} + h^+ + e^-$$

(ii) Formation of hydroxyl radicals.

$$H_2O_2 + e^- \rightarrow OH^- + \bullet OH$$

(iii) Degradation of AFG1 or AFG2.

$$\text{AFG1 or AFG2} + \bullet OH \rightarrow \text{Degradation products } (CO_2, H_2O, \text{etc.})$$

Catalyst reusability

The reusability of photocatalysts is essential for sustainable and cost-effective environmental remediation processes. In the context of using the Bimetallic MIL-53 (Al, Ni)/ZnO NPs composite for the degradation of AFG1 and AFG2, ensuring its reusability can greatly improve the efficiency and practicality of the treatment method. This, in turn, helps minimize resource consumption, reduce waste generation, and ultimately lower the overall operational costs of the degradation process. To assess the reusability of the Bimetallic MIL-53 (Al, Ni)/ZnO NPs composite as a photocatalyst, investigations were carried out under optimal conditions. After employing the composite in the photodegradation of AFG1 and AFG2, the catalyst was isolated from the solution, washed with distilled water, and dried at 60 °C for reuse. The results, presented in Table 7 and Fig. 9, demonstrate that the Bimetallic MIL-53 (Al, Ni)/ZnO NPs composite can be used for five cycles of AFG1 and AFG2 degradation

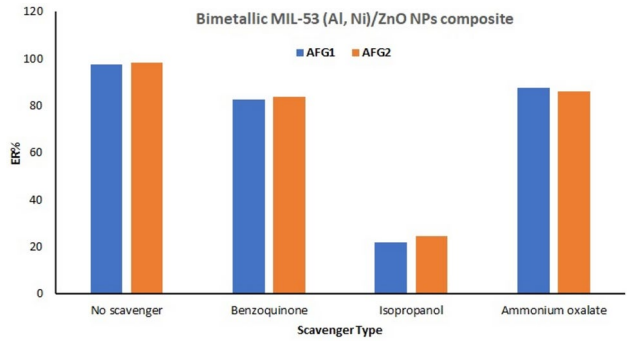

Fig. 8. The effect of scavengers on AFG1 and AFG2 degradation using the Bimetallic MIL-53 (Al, Ni)/ZnO NPs.

Cycle	AFG1	AFG2
1	97.26 ± 2.06	98.44 ± 1.89
2	96.89 ± 2.11	97.73 ± 2.03
3	95.66 ± 2.54	96.59 ± 2.27
4	93.27 ± 2.84	95.27 ± 2.31
5	91.06 ± 3.06	93.21 ± 2.45
6	86.32 ± 3.11	87.56 ± 2.76

Table 7. Reusability of the Bimetallic MIL-53 (Al, Ni)/ZnO NPs composite as a photocatalyst for degradation of AFG1 and AFG2.

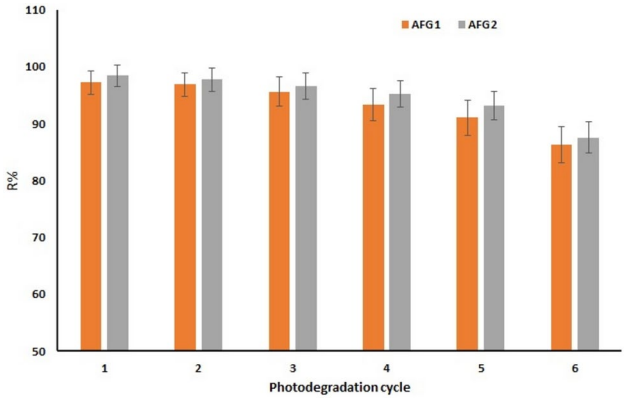

Fig. 9. The reusability of the photocatalyst to degrade AFG1 and AFG2.

without a significant decrease in its effectiveness. This indicates that the prepared photocatalyst exhibits favorable stability as a catalyst in the degradation process of AFG1 and AFG2.

Real sample investigation

To assess the photocatalyst's efficacy in real-world conditions, river water (Mayan River, Torqebah, Iran) and well water (Mashhad suburb, Iran) samples were collected. Ten replicate samples (500 mL each) were collected hourly over a single day from each source, pooled, and analyzed for AFG1 and AFG2. Initial AFG1 and AFG2 concentrations were below the method's detection limit in both water sources. Subsequently, 500 mL aliquots of each pooled sample were spiked with AFG1 and AFG2 standard solutions to achieve a final concentration of 35 mg/L. These spiked samples were then subjected to the photodegradation process. The resulting AFG1 and AFG2 removal efficiencies were high in both river and well water samples: river water, 97.1 ± 1.6% and 97.8 ± 1.9% for AFG1 and AFG2, respectively; and well water, 97.3 ± 1.9% and 98.3 ± 1.8% for AFG1 and AFG2, respectively. These results demonstrate the effectiveness of the photocatalytic method for removing AFG1 and AFG2 in real water matrices.

Conclusion

This study demonstrates the efficient photodegradation of AFG1 and AFG2 using a novel Bimetallic MIL-53 (Al, Ni)/ZnO NPs composite as a photocatalyst. The optimized conditions for the degradation process, including pH, photocatalyst and aflatoxin concentrations, and H_2O_2 concentration, were identified using an experimental design based on the central composite design. The optimal values of pH, photocatalyst amount, concentration of AFs, and H_2O_2 concentration were 4.1, 109 mg, 35 mgL^{-1}, and 3 mM, respectively. The predicted removal efficiencies for AFG1 and AFG2 under the optimum conditions in the presence of the composite as a photocatalyst were high, indicating the effectiveness of the composite. Kinetic studies revealed the rate constants and half-life times for the photodegradation of AFG1 and AFG2, further confirming the procedure's suitability. The pseudo-first-order rate constants of 0.058 ± 0.002 min^{-1} and 0.060 ± 0.003 min^{-1} were obtained for the removal of AFG1 and AFG2, respectively. Furthermore, the composite exhibited excellent reusability, maintaining its efficacy even after five cycles of AFG1 and AFG2 degradation without a significant decrease in its effectiveness. These findings highlight the potential of the Bimetallic MIL-53 (Al, Ni)/ZnO NPs composite as a stable and efficient photocatalyst for the removal of aflatoxins G1 and G2, making it highly suitable for practical applications in environmental remediation processes.

Data availability

All data generated or analyzed during this study are included in this published article.

Received: 6 January 2025; Accepted: 17 March 2025
Published online: 01 April 2025

References

1. Awuchi, C. G. et al. Aflatoxins in foods and feeds: A review on health implications, detection, and control. *Bull. Environ. Pharmacol. Life Sci* **9**, 149–155 (2020).
2. Khan, R., Ghazali, F. M., Mahyudin, N. A. & Samsudin, N. I. P. Biocontrol of aflatoxins using non-aflatoxigenic Aspergillus flavus: A literature review. *Journal of Fungi* **7**, 381 (2021).
3. Benkerroum, N. Chronic and acute toxicities of aflatoxins: Mechanisms of action. *Int. J. Environ. Res. Public Health* **17**, 423 (2020).
4. Valencia-Quintana, R. et al. Environment changes, aflatoxins, and health issues, a review. *Int. J. Environ. Res. Public Health* **17**, 7850 (2020).
5. Fouché, T. C. *Ecotoxicological assessment of aflatoxin in soil under different temperature and moisture conditions utilising earthworms* (North-West University (South Africa), 2022).
6. Bansal, A.; Sharma, M.; Pandey, A.; Shankar, J. Aflatoxins: occurrence, biosynthesis pathway, management, and impact on health. In *Fungal Resources for Sustainable Economy: Current Status and Future Perspectives, Springer*. 565–594 (2023).
7. Michelin, E. et al. Long-term exposure of Pacu (Piaractus mesopotamicus) fish to dietary aflatoxin B1: residues in tissues and performance. *World Mycotoxin J.* **14**, 411–419 (2021).
8. Cao, W., Yu, P., Yang, K. & Cao, D. Aflatoxin B1: Metabolism, toxicology, and its involvement in oxidative stress and cancer development. *Toxicol. Mech. Methods* **32**, 395–419 (2022).
9. Ismail, A. et al. Early life exposure to dietary aflatoxins, health impact and control perspectives: A review. *Trends Food Sci. Technol.* **112**, 212–224 (2021).
10. Imran, M. et al. Mycotoxins–a global one health concern: A review. *Agrobiol Rec.* **2**, 1–16 (2020).
11. Moslehi, M. H. et al. Photocatalytic decomposition of metronidazole by zinc hexaferrite coated with bismuth oxyiodide magnetic nanocomposite: Advanced modelling and optimization with artificial neural network. *Chemosphere* **356**, 141770 (2024).
12. Ghorbani, M., Seyedin, O. & Aghamohammadhassan, M. Adsorptive removal of lead (II) ion from water and wastewater media using carbon-based nanomaterials as unique sorbents: A review. *J. Environ. Manage.* **254**, 109814. https://doi.org/10.1016/j.jenvman.2019.109814 (2020).
13. Moghaddam, N. S. M. et al. Application of magnetic activated carbon coated with CuS nanoparticles as a new adsorbent for the removal of tetracycline antibiotic from aqueous solutions (isotherm, kinetic and thermodynamic study). *Desalin. Water Treat.* **280**, 297–311 (2022).
14. Moslehi, M. H. et al. Statistical computational optimization approach for photocatalytic-ozonation decontamination of metronidazole in aqueous media using CuFe2O4/SiO2/ZnO nanocomposite. *Environ. Res.* **242**, 117747. https://doi.org/10.1016/j.envres.2023.117747 (2024).
15. Prabhakar, U. P. S. et al. Non-covalent functionalization of surfactant-assisted graphene oxide with silver nanocomposites for highly efficient photocatalysis and anti-biofilm applications. *Mater. Sci. Energy Technol.* **7**, 205–215. https://doi.org/10.1016/j.mset.2023.10.005 (2024).
16. Azqandi, M. et al. Innovative RGO-bridged S-scheme CuFe2O4@ Ag2S heterojunction for efficient Sun-light-driven photocatalytic disintegration of Ciprofloxacin. *Carbon* **231**, 119725 (2025).
17. Nasseh, N. et al. Integrated Fenton-like and photocatalytic system for metronidazole degradation in water using FeNi3/SiO2/CuS magnetic nanocomposite. *Desalin. Water Treat.* **303**, 160–170 (2023).
18. Azqandi, M. et al. Intensified photo-decontamination of tetracycline antibiotic by S-scheme spinel manganese ferrite-grafted ZIF-8 heterojunction photocatalyst: Mechanism conception, degradation pathway and DFT studies. *J. Environ. Chem. Eng.* **12**, 112875 (2024).
19. Shanmugam, P. et al. Hydrothermal synthesis and photocatalytic application of ZnS-Ag composites based on biomass-derived carbon aerogel for the visible light degradation of methylene blue. *Environ. Geochem. Health* **46**, 92 (2024).
20. Hossein Panahi, A., Al-Musawi, T. J., Masihpour, M., Fard, S. F. T. & Nasseh, N. Photocatalytic degradation of humic acid using bentonite@ Fe3O4@ ZnO magnetic nanocomposite: An Investigation of the characterization of the photocatalyst, degradation pathway, and modeling by solver plugin. *Water* **15**, 2931 (2023).
21. Abdarnezhadi, R. & Mehrizad, A. Flowerlike Sm–ZnIn2S4 as a Susceptible Visible-Light Photocatalyst for Cr6+ Reduction: Experimental design, RSM, and ANN modeling. *J. Inorg. Organomet. Polymers Mater.* **33**, 1621–1637. https://doi.org/10.1007/s10904-023-02586-z (2023).
22. Bagherlou, N., Ghasemi, E., Gharbani, P., Babazadeh, M. & Mehrizad, A. Optimization and modeling of betamethasone removal from aqueous solutions using a SiO2/g-C3N5@NiFe2O4 nanophotocatalyst by RSM. *npj Clean Water* https://doi.org/10.1038/s41545-023-00295-1 (2024).
23. Yeganeh, M., Charkhloo, E., Sobhi, H. R., Esrafili, A. & Gholami, M. Photocatalytic processes associated with degradation of pesticides in aqueous solutions: Systematic review and meta-analysis. *Chem. Eng. J.* **428**, 130081. https://doi.org/10.1016/j.cej.2021.130081 (2022).
24. Shen, M.-H. & Singh, R. K. Detoxification of aflatoxins in foods by ultraviolet irradiation, hydrogen peroxide, and their combination-a review. *Lwt* **142**, 110986 (2021).
25. Parasuraman, B. et al. Photocatalytic degradation of tetracycline contaminated wastewater over Bi2S3/BiWO6/rGO ternary nanocomposite under visible light irradiation. *J. Taiwan Inst. Chem. Eng.* https://doi.org/10.1016/j.jtice.2023.105249 (2023).
26. Azqandi, M., Shahryari, T., Nasseh, N. & Fanaei, F. Green synthesis of MnFe2O4 magnetic nanoparticle and its application in photocatalytic degradation of tetracycline Antibiotic: An Effective model for wastewater treatment of military pharmaceutical industries. *Mil. Caring Sci. J.* **10**, 3 (2023).
27. Mehrizad, A. & Gharbani, P. Synthesis of ZnS decorated carbon fibers nanocomposite and its application in photocatalytic removal of Rhodamine 6G from aqueous solutions. *Prog. Color, Colorants Coat.* **10**, 13–21 (2017).
28. Nasseh, N., Moghaddam, N. S. M., Barikbin, B. & Khosravi, R. Excellent driven rapid photocatalytic activity with high reusable magnetic nanocomposite in tetracycline degradation under simulated sunlight. *Desalin. Water Treat.* **291**, 148–162 (2023).
29. Rahimi, S. M., Arghavan, F. S., Othmani, A. & Nasseh, N. Magnetically recoverable nickel ferrite coated with CuS nanocomposite for degradation of metronidazole in photocatalytic and photo fenton like processes. *Int. J. Environ. Anal. Chem.* **102**, 6699–6719 (2022).
30. Guo, Y., Zhao, L., Ma, Q. & Ji, C. Novel strategies for degradation of aflatoxins in food and feed: A review. *Food Res. Int.* **140**, 109878 (2021).
31. Song, C. et al. Mechanisms and transformed products of aflatoxin B1 degradation under multiple treatments: A review. *Crit. Rev. Food Sci. Nutr.* **64**, 2263–2275 (2024).
32. Singh, P. & Borthakur, A. A review on biodegradation and photocatalytic degradation of organic pollutants: A bibliometric and comparative analysis. *J. Clean. Prod.* **196**, 1669–1680 (2018).
33. Hossein Panahi, A., Al-Musawi, T. J., Masihpour, M., Fard, S. F. T. & Nasseh, N. Photocatalytic degradation of humic acid using Bentonite@Fe3O4@ZnO Magnetic Nanocomposite: An investigation of the characterization of the photocatalyst, degradation pathway, and modeling by solver plugin. *Water* **15**, 2931 (2023).

34. Ngullie, R. C. et al. Magnetically recoverable Biomass-Derived Carbon-Aerogel supported ZnO (ZnO/MNC) composites for the photodegradation of methylene blue. *Catalysts* **12**, 1073 (2022).
35. Mazari Moghaddam, N. S., Al-Musawi, T. J., Arghavan, F. S. & Nasseh, N. Effective removal of Sirius yellow K-CF dye by adsorption process onto chitosan-polyacrylamide composite loaded with ZnO nanoparticles. *Int. J. Environ. Anal. Chem.* **103**, 8782–8798 (2023).
36. Yeganeh, M., Sobhi, H. R., Behbahani, M., Ghambarian, M. & Esrafili, A. Photoelectrocatalytic degradation of sulphonamide antibiotics in aquatic media using a novel Co-doped ZnO nanocomposite: evaluation of performance, kinetic studies. *Int. J. Environ. Anal. Chem.* **104**, 2304–2315. https://doi.org/10.1080/03067319.2022.2060092 (2024).
37. Sanakousar, F., Vidyasagar, C., Jiménez-Pérez, V. & Prakash, K. Recent progress on visible-light-driven metal and non-metal doped ZnO nanostructures for photocatalytic degradation of organic pollutants. *Mater. Sci. Semicond. Process.* **140**, 106390 (2022).
38. Shanmugam, P. et al. Visible-light induced photocatalytic removal of methylene blue dye by copper oxide decorated zinc oxide nanorods. *Mater. Sci. Energy Technol.* **6**, 359–367. https://doi.org/10.1016/j.mset.2023.03.001 (2023).
39. Arora, I., Chawla, H., Chandra, A., Sagadevan, S. & Garg, S. Advances in the strategies for enhancing the photocatalytic activity of TiO2: Conversion from UV-light active to visible-light active photocatalyst. *Inorg. Chem. Commun.* **143**, 109700 (2022).
40. Azqandi, M., Ramavandi, B., Nasseh, N., Zaarei, D. & Fanaei, F. Green synthesis of manganese ferrite magnetic nanoparticle and its modification with metallic-organic frameworks for the tetracycline adsorption from aqueous solutions: A mathematical study of kinetics, isotherms, and thermodynamics. *Environ. Res.* **256**, 118957. https://doi.org/10.1016/j.envres.2024.118957 (2024).
41. Azqandi, M., Shahryari, T., Fanaei, F. & Nasseh, N. Green construction of magnetic MnFe2O4/ZIF-8 nanocomposite utilizing extract of Melissa officinalis plant for the photo-degradation of tetracycline under UV illumination. *Catalysis Commun.* **185**, 106798 (2023).
42. Yeganeh, M. et al. Utilization of the copper recovered from waste printed circuit boards as a metal precursor for the synthesis of TiO2/magnetic-MOF(Cu) nanocomposite: Application in photocatalytic degradation of pesticides in aquatic solutions. *J. Environ. Manage.* **345**, 118755. https://doi.org/10.1016/j.jenvman.2023.118755 (2023).
43. Abbasnia, A. et al. Removal of tetracycline antibiotics by adsorption and photocatalytic-degradation processes in aqueous solutions using metal organic frameworks (MOFs): A systematic review. *Inorg. Chem. Commun.* **145**, 109959. https://doi.org/10.1016/j.inoche.2022.109959 (2022).
44. Ghorbani, M. et al. Crafting an Innovative Bimetallic MOF-on-MOF/TiO2 Composite for Effective Removal of Imatinib Anticancer Agent through Adsorption and Photodegradation. *Sep. Purif. Technol.* **336**, 126227 (2024).
45. Ghorbani, M. et al. Advancements, Applications, and prospects of Metal-Organic frameworks and their derivatives as distinct sorbents in exhaustive and non-exhaustive extraction strategies. *Microchem. J.* **198**, 110158 (2024).
46. Yeganeh, M., Sobhi, H. R. & fallah S. Ghambarian M, Esrafili A.,. Sono-assisted photocatalytic degradation of ciprofloxacin in aquatic media using g-C3N4/MOF-based nanocomposite under visible light irradiation. *Environ. Sci. Pollut. Res.* **31**, 35811–35823. https://doi.org/10.1007/s11356-024-33222-z (2024).
47. Ghorbani, M. et al. Optimization and synthesis of a novel sorbent composite based on magnetic chitosan-amine-functionalized bimetallic MOF for the simultaneous dispersive solid-phase microextraction of four aflatoxins in real water, herbal distillate, and food samples. *Anal. Bioanal. Chem.* **415**, 5681–5694. https://doi.org/10.1007/s00216-023-04842-0 (2023).
48. Keshavarzi, M. et al. Development of a magnetic sorbent based on synthesis of MOF-on-MOF composite for dispersive solid-phase microextraction of five phthalate esters in bottled water and fruit juice samples. *Microchemical J.* **182**, 107934 (2022).
49. Liu, Z. et al. Study of photodegradation kinetics of aflatoxins in cereals using trilinear component modeling of excitation-emission matrix fluorescence data. *Spectrochimica Acta Part A: Mol. Biomol. Spectrosc.* **235**, 118266 (2020).
50. Sun, S., Zhao, R., Xie, Y. & Liu, Y. Reduction of aflatoxin B1 by magnetic graphene oxide/TiO2 nanocomposite and its effect on quality of corn oil. *Food Chem.* **343**, 128521 (2021).
51. Nisa, M. U., Bilhod, W. & Insin, N. Selective photodegradation of aflatoxin B1 in chili oil using titania-silica-iron oxide nanocomposites with molecularly imprinted technology. *Inorganic Chem. Commun.* **173**, 113883 (2025).
52. Raesi, S. et al. Photocatalytic detoxification of aflatoxin B1 in an aqueous solution and soymilk using nano metal oxides under UV light: Kinetic and isotherm models. *Lwt* **154**, 112638 (2022).
53. Ghorbani, M. et al. Crafting an innovative bimetallic MOF-on-MOF/TiO2 composite for effective removal of Imatinib anticancer agent through adsorption and photodegradation. *Sep. Purifi. Technol.* **336**, 126227. https://doi.org/10.1016/j.seppur.2023.126227 (2024).
54. Shi, S. et al. Photothermal-boosted effect of binary CuFe bimetallic magnetic MOF heterojunction for high-performance photo-Fenton degradation of organic pollutants. *Sci. Total Environ.* **795**, 148883 (2021).
55. Shan, C. et al. Preparation and application of bimetallic mixed ligand MOF photocatalytic materials. *Colloids and Surfaces A: Physicochem. Eng. Aspects* **636**, 128108 (2022).
56. Mohan, S., Vellakkat, M., Aravind, A. & Reka, U. Hydrothermal synthesis and characterization of Zinc Oxide nanoparticles of various shapes under different reaction conditions. *Nano Express* **1**, 030028 (2020).
57. Ahadi, N., Askari, S., Fouladitajar, A. & Akbari, I. Facile synthesis of hierarchically structured MIL-53 (Al) with superior properties using an environmentally-friendly ultrasonic method for separating lead ions from aqueous solutions. *Sci. Rep.* **12**, 2649 (2022).
58. Amarzadeh, M. et al. Heterogeneous Fenton-like photocatalytic process towards the eradication of tetracycline under UV Irradiation: Mechanism elucidation and environmental risk analysis. *Water* **15**, 2336 (2023).
59. Ghorbani, M. et al. Investigation and Health Risk Assessment of Nitrate ion Nitriteion and Phthalate Esters in Herbal Distillates Produced by Iranian Companies. *Fine Chem. Eng.* https://doi.org/10.37256/fce.5120243344 (2024).

Acknowledgements

The authors would like to thank Payame Noor University, Tehran, Iran, for financial support.

Author contributions

Shiva Teilaghi: Formal analysis, Validation, Data curation, Writing e original draft, Resources. Zinat Gordi: Conceptualization, Methodology, Supervision, Writing e review & editing, Investigation, Resources.

Declarations

Competing interests

The authors declare no competing interests.

Ethical approval

This article does not contain any studies with human or animal subjects.

Additional information

Correspondence and requests for materials should be addressed to Z.G.